Engineering Structures 302 (2024) 117450

Contents lists available at ScienceDirect

Engineering Structures

journal homepage: www.elsevier.com/locate/engstruct

Vibration control of offshore wind turbines with a novel energy-adaptive self-powered active mass damper

Jin-Yang LI [a,b], Songye ZHU [b], Jian ZHANG [b], Ruisheng MA [c], Haoran ZUO [d,*]

[a] State Key Laboratory of Coastal and Offshore Engineering, Dalian University of Technology, Dalian 116023, China
[b] Department of Civil and Environmental Engineering, The Hong Kong Polytechnic University, Kowloon, Hong Kong, China
[c] Key Laboratory of Urban Security and Disaster Engineering of Ministry of Education, Beijing University of Technology, Beijing 100124, China
[d] Centre for Infrastructural Monitoring and Protection, School of Civil and Mechanical Engineering, Curtin University, Kent Street, Bentley WA 6102, Australia

A R T I C L E I N F O

Keywords:
Offshore wind turbines
Vibration control
Energy harvesting
Self-powered active mass dampers

A B S T R A C T

Slender and flexible offshore wind turbines (OWTs) are vulnerable to external dynamic excitations, and passive tuned mass dampers (TMDs) have been widely used to control excessive vibrations of OWTs under harsh marine environments (e.g., strong winds and irregular sea waves). However, TMDs are only effective in the vicinity of the controlled frequency, i.e., in a narrow frequency band. Compared to passive TMDs, active control methods are normally considered to possess better control performances but at the cost of a large amount of external energy input. To this end, the present study proposes a novel energy-adaptive self-powered active mass damper (SPAMD) to mitigate the responses of OWT towers. The proposed control device can harvest energies from OWTs and then use them as the power to drive an active mass damper for structural vibration control. Specifically, a representative OWT is selected as a prototype structure and its tower is modeled as a multi-degree-of-freedom system by simplifying the rotor-nacelle assembly as a lumped mass and moment of inertia. The dynamic characteristics (mainly natural frequency and mode shape) of the tower obtained by the developed model are validated against a finite element model. Subsequently, the system configuration and working mechanism of SPAMD are introduced and SPAMD is incorporated into the developed model to simultaneously harvest energy and mitigate the fore-aft responses of the tower under wind and sea wave loads. The control effectiveness of SPAMD is further compared to the traditional TMD. Results show that SPAMD has a superior effect over TMD in controlling OWT responses.

1. Introduction

With the global emphasis on sustainable development and carbon neutrality for the next generation, better utilization of green energy sources is drawing increasing attention nowadays, especially wind energy. In 2022, a total of 77.6 GW of new wind power installations were added worldwide, bringing the cumulative installed wind capacity to 906 GW, and offshore wind accounted for approximately 8.8 GW [1]. Multi-megawatt offshore wind turbines (OWTs) with extremely long blades and slender towers are generally designed and constructed in deep seas to generate more power in all wind speed conditions and to dramatically lower the levelized cost of electricity. Deep sea areas are usually associated with complex wind and wave conditions, and these slender and flexible wind energy structures are more vulnerable to external dynamic excitations. Excessive vibrations in OWTs have various detrimental effects, including compromising power production, increasing maintenance and operational costs, reducing fatigue life, and potentially resulting in structural failures. Therefore, it is imperative to control OWT responses for structural functionality and safety.

The operational range of a wind turbine is typically divided into two regions based on wind speed: below and above the rated wind speed. When below the rated wind speed, the wind turbine operates at variable rotor speed to extract the maximum power available from the wind, and the torque control is activated to regulate the rotor speed. In the above-rated wind speed conditions, the primary objective is to maintain a constant power output, which is generally achieved by employing pitch control to vary the blade pitch angle. The purpose of pitch control is to reduce the aerodynamic loads (i.e., external excitations) on the blades and to protect the wind turbine from damage at high wind speeds. Structural vibration control, on the other hand, is sophisticated and

* Corresponding author.
E-mail address: haoran.zuo@curtin.edu.au (H. ZUO).

https://doi.org/10.1016/j.engstruct.2024.117450
Received 17 July 2023; Received in revised form 14 December 2023; Accepted 31 December 2023
Available online 9 January 2024

commonly studied in wind turbines. It is worth noting that structural vibration control methods are independent of existing control techniques of wind turbines (i.e., torque and pitch control), and they essentially function following the prescribed control algorithms. Structural vibration control is generally categorized as passive, semi-active, and active control types based on the amount of energy input and the requirement of feedback loops [2]. Passive control devices, among various options, attract significant attention primarily due to zero energy input and easy implementation features, and some representatives are tuned mass dampers (TMDs) [3], tuned liquid dampers (TLDs) [4], tuned liquid column dampers (TLCDs) [5], and their variants. Their effectiveness in mitigating responses of wind turbines has been numerically and/or experimentally demonstrated. Hemmati et al. [6] utilized a combined TMD-TLCD in the nacelle to control the tower responses under different working conditions, and their results highlighted that TMDs were more effective in operational conditions while TLCDs had better performances in parked conditions. Sun and Jahangiri [7,8] used a three-dimensional (3D) pendulum TMD to reduce tower responses in both fore-aft and side-to-side directions induced by wind-wave misalignment, and the 3D pendulum TMD was later integrated with a linear energy harvester to replace viscous damper [9] and with visco-elastic material to develop a 3D pounding pendulum TMD [10], individually. Liu et al. [11] designed a spring pendulum pounding TMD to increase the damping in the lateral (side-to-side) direction of towers. A prestressed TMD was proposed by Liu et al. [12] and Lei et al. [13] to reduce tower responses under seismic and combined aerodynamic and hydrodynamic loads, respectively. Ding et al. [14] designed a toroidal TLCD to simultaneously control multi-hazard (wind, wave, and seismic loads) responses of towers in both fore-aft and side-to-side directions. Zhang et al. [15] and Chen et al. [16] added an inerter into linear spring and viscous damping elements to reduce seismic responses of towers, and their results demonstrated that inerter-based dynamic vibration absorbers with a smaller mass ratio could achieve the same control effectiveness as TMD. Kampitsis et al. [17] introduced a negative stiffness element into the traditional TMD to form an extended KDamper and it had a good vibration absorption capability without increasing the secondary mass at the top of the tower.

Notably, the frequency of a passive control device is usually tuned to the vicinity of the primary structure's target natural frequency to achieve optimal control performance (i.e., narrow effective frequency band). When the device frequency is slightly mistuned from that of the controlled structure, its effectiveness may significantly deteriorate, or even amplify the structural response which is indeed undesired. With the advancement of design methods and construction techniques, OWTs move farther from coastlines and are installed in deep seas that have complex seabed conditions and harsh environmental loads, and therefore, their dynamic characteristics (mainly natural frequency) inevitably change due to foundation-soil interaction, discrepancies between design, manufacture, and construction, operational conditions (rotor dynamics [18]), and material property degradation and structural damage during their whole lifetime. Dai et al. [19] and Lin et al. [20] performed scaled experimental tests to investigate the foundation-soil interaction on the control effectiveness of TMDs and their results showed that TMD partially lost the capability to reduce tower responses. Therefore, semi-active and active control methods have been adopted to mitigate vibrations of wind turbine blades (e.g., [21–26]) and towers. Sun [27,28], and Hemmati and Oterkus [29] used a semi-active TMD to mitigate tower responses induced by multiple hazards considering the soil effects and structural damage. Sarkar and Chakraborty [30,31] developed a semi-active strategy using multiple magneto-rheological TLCDs to mitigate excessive vibrations of towers. Fitzgerald et al. [32], Hu et al. [33], and Brodersen et al. [34] used an active tuned mass damper (ATMD) to improve the structural performances of wind turbines, and the results demonstrated that ATMD could be used to further reduce tower responses compared with passive TMDs [34].

Nevertheless, the conventional perception concludes that semi-active and active control strategies achieve enhanced vibration control performance over passive control at the cost of high energy consumption, and this external energy input further raises potential instability concerns (e.g., vibration amplification due to overall external energy input caused by potential time lag, etc.), which prohibits its wider applications in civil structures (including OWTs). However, this situation is substantially eased by the recent advances in self-powered active control techniques [35–37], where full-loop active control performance can be readily accomplished without requiring an external power supply at all (i.e., zero power consumption like passive control). However, the existing self-powered active control approach uses a two-node control device, limiting its applications in monopile-support structures (e.g., OWTs).

To this end, the present study will propose a novel energy-adaptive self-powered active mass damper (SPAMD) taking advantage of existing self-powered active control techniques and further widening its application range by enabling single-node connection mode. Subsequently, a thorough feasibility analysis of the effectiveness of SPAMD in controlling the vibrations of a benchmark OWT will be carried out. In addition to the introduction of system topology and working mechanism, a novel energy-adaptive self-powered active control algorithm that is perfectly compatible with SPAMD and meanwhile guarantees long-term optimal active control will also be covered. Finally, a control performance comparison between the scenarios using traditional TMD and SPAMD individually will be conducted based on the numerical simulation results, which is expected to highlight the merits of SPAMD.

2. Description of OWT with SPAMD system

2.1. OWT model

The commonly used NREL 5 MW wind turbine [38] in academia is chosen as the benchmark OWT in the present study, and Table 1 presents its detailed information. As reported in [38], the wall thickness of the tower is increased by 30% to ensure that the first eigenfrequency of the tower is within one and three times the rotating frequency in the whole operational range. Moreover, the outer diameter and thickness of the tower are linearly decreased from the tower base to the top. The tower and monopile are made of steel, and the density and elastic modulus of steel are 8500 kg/m^3 and 210 GPa, respectively [38].

The responses of the wind turbine tower along the wind direction (referred to as the fore-aft direction) are relatively large and the vibrations in that direction are the target to be mitigated. Therefore, the present study aims to design a novel energy-adaptive SPAMD and to investigate its effectiveness in controlling the fore-aft responses of the tower when subjected to stochastic wind and sea wave loads. Only the tower and monopile are modeled by a multi-degree-of-freedom (MDOF)

Table 1
Information on the NREL 5 MW OWT.

Basic description	Cut-in, rated, and cut-out wind speed	3 m/s, 11.4 m/s, and 25 m/s
	Cut-in and rated rotor speed	6.9 rpm and 12.1 rpm
Blade	Length	61.5 m
	Overall (Integrated) mass	17,740 kg
	Second mass moment of inertia (w.r.t. root)	11,776,047 kg·m^2
Hub and nacelle	Hub diameter and height	3 m and 90 m
	Hub mass	56,780 kg
	Nacelle mass	240,000 kg
Tower	Length	87.6 m
	Overall (Integrated) mass	347,460 kg
	Base diameter and thickness	6 m and 0.027 m
	Top diameter and thickness	3.87 m and 0.019 m
	Structural damping ratio	1%
Monopile	Length	20 m
	Diameter and thickness	6 m and 0.06 m

system consisting of Euler-Bernoulli beam elements, and the rotor-nacelle assembly (i.e., three blades, hub, and nacelle) is considered an additional mass with a mass moment of inertia located at the top of the tower.

Fig. 1 shows the discretization of the tower and monopile. The tower and the monopile foundation are divided into 22 elements from the monopile base to the tower top, based on several trials to balance the computational accuracy and efficiency. The element length is 5 m for the first 21 elements and 2.76 m for the last element. The translational and rotational degree-of-freedoms (DOFs) at each element node are considered for a total of 44 DOFs. As the monopile and tower are composed of hollow and circular cross-sections, the mass and mass moment of inertia at cross-sections and the sectional flexural stiffness in the fore-aft direction along the height of the monopile and tower can be calculated according to the geometries, material density, and elastic modulus. In particular, the mass and mass moment of inertia at an element node are the calculated values at cross-sections times the sum of the halves of the lengths of two adjacent elements to generate the global mass matrix $\boldsymbol{M}_{\text{OWT}}(\in \mathbb{R}^{44\times 44})$of the wind turbine, which can be expressed by

$$\boldsymbol{M}_{\text{OWT}} = \begin{bmatrix} m_1 & & & & & & & \\ & J_1 & & & & & & \\ & & \ddots & & & & & \\ & & & m_i & & & & \\ & & & & J_i & & & \\ & & & & & \ddots & & \\ & & & & & & m_{22}+m_{\text{RNA}} & \\ & & & & & & & J_{22}+J_{\text{RNA}} \end{bmatrix} \tag{1}$$

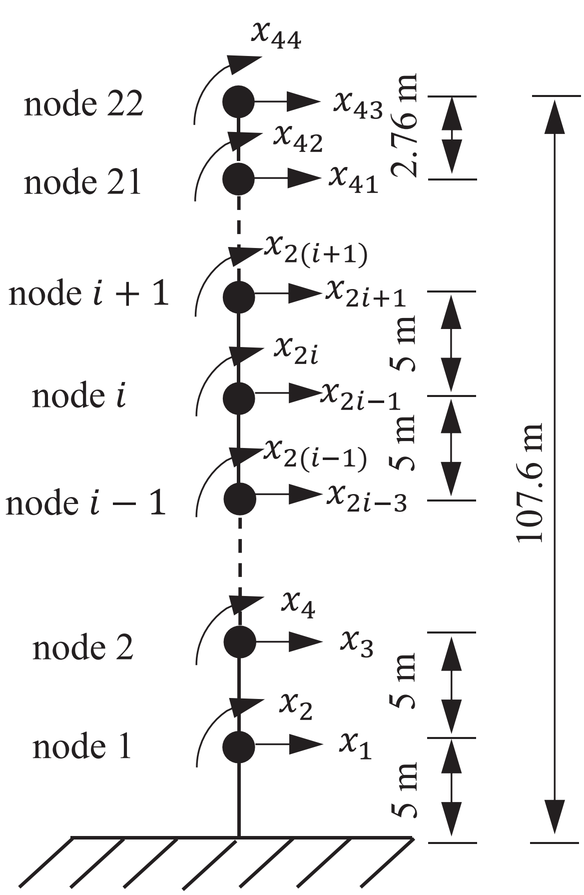

Fig. 1. Analytical model of OWT.

where m_i and J_i are the mass and mass moment of inertia at a node i, m_{RNA}, J_{RNA} are the mass and mass moment of inertia of the rotor-nacelle assembly.

The stiffness matrix of an element i ($\boldsymbol{k}_i^e \in \mathbb{R}^{4\times 4}$) is

$$\boldsymbol{k}_i^e = \begin{bmatrix} \frac{12(EI)_i}{l_i^3} & \frac{6(EI)_i}{l_i^2} & -\frac{12(EI)_i}{l_i^3} & \frac{6(EI)_i}{l_i^2} \\ \frac{6(EI)_i}{l_i^2} & \frac{4(EI)_i}{l_i} & -\frac{6(EI)_i}{l_i^2} & \frac{2(EI)_i}{l_i} \\ -\frac{12(EI)_i}{l_i^3} & -\frac{6(EI)_i}{l_i^2} & \frac{12(EI)_i}{l_i^3} & -\frac{6(EI)_i}{l_i^2} \\ \frac{6(EI)_i}{l_i^2} & \frac{2(EI)_i}{l_i} & -\frac{6(EI)_i}{l_i^2} & \frac{4(EI)_i}{l_i} \end{bmatrix} \tag{2}$$

where $(EI)_i$ is the flexural stiffness of an element i, and it is defined as the average of the sectional flexural stiffness between two adjacent cross-sections; l_i is the element length. The global stiffness matrix $\boldsymbol{K}_{\text{OWT}}(\in \mathbb{R}^{44\times 44})$ of the OWT is achieved by assembling these element stiffness matrices.

After establishing the structural mass and stiffness matrices, an eigenvalue analysis is carried out to calculate the natural frequencies and mode shapes of the tower. Table 2 tabulates the frequencies corresponding to the first and second vibration modes of the tower, and the mode shapes are shown in Fig. 2. In addition, they are also compared to those from ABAQUS, in which the same OWT is modeled using two-dimensional Euler-Bernoulli beam elements. As shown, the natural frequencies and mode shapes of the present model agree well with those in ABAQUS, indicating the accuracy of the developed model in the present study. Rayleigh damping is adopted to develop the structural damping matrix $\boldsymbol{C}_{\text{OWT}}(=\alpha\boldsymbol{M}_{\text{OWT}}+\beta\boldsymbol{K}_{\text{OWT}}, \in \mathbb{R}^{44\times 44})$, and parameters α and β are the mass and stiffness coefficients, respectively. A damping ratio of 1% [38] has been assigned to the first and second vibration modes of the tower, and the values of α and β are 0.0309 and 0.0014, respectively [39].

Fig. 3 shows the schematic of OWT with SPAMD, and the wind and sea wave loads are acting in the fore-aft direction of the tower in the present study. The equation of motion of the OWT with SPAMD can be expressed by

$$\boldsymbol{M}\ddot{\boldsymbol{x}} + \boldsymbol{C}\dot{\boldsymbol{x}} + \boldsymbol{K}\boldsymbol{x} = \boldsymbol{\gamma}\cdot f_{\text{ctrl}} + \boldsymbol{w} \tag{3}$$

where $\boldsymbol{x} = [x_1, x_2\cdots x_{44}, x_a]^T$ is the transverse displacement vector and x_a is the displacement at the active mass location; and the global mass, damping, and stiffness matrices are in the form of $\boldsymbol{M}_{45\times 45} = [\boldsymbol{M}_{\text{OWT}}, \boldsymbol{0}; \boldsymbol{0}, m_a]$, $\boldsymbol{C}_{45\times 45} = [\boldsymbol{C}_{\text{OWT}}, \boldsymbol{0}; \boldsymbol{0}, c_a]$, $\boldsymbol{K}_{45\times 45} = [\boldsymbol{K}_{\text{OWT}}, \boldsymbol{0}; \boldsymbol{0}, k_a]$, respectively, where m_a, k_a, and c_a are the corresponding parameters of SPAMD; $\boldsymbol{\gamma}$ defines the location of the control force, f_{ctrl} is the control force generated by SPAMD, $\boldsymbol{w}$ is the discretized external wind and sea wave forces along the height of the monopile and tower (i.e., vertical direction). Besides, since SPAMD is a single-node device, the generated active control force to the tower top (nacelle) can be written as

$$f_{\text{ctrl}} = -m_a\ddot{x}_a \tag{4}$$

where m_a and $\ddot{x}_a$ are the mass and the absolute acceleration of the active mass, respectively.

Table 2
Natural frequencies of the tower.

Mode	Present model (rad/s)	ABAQUS (rad/s)	Difference
First	1.7658	1.7628	0.17%
Second	12.3094	12.2230	0.71%

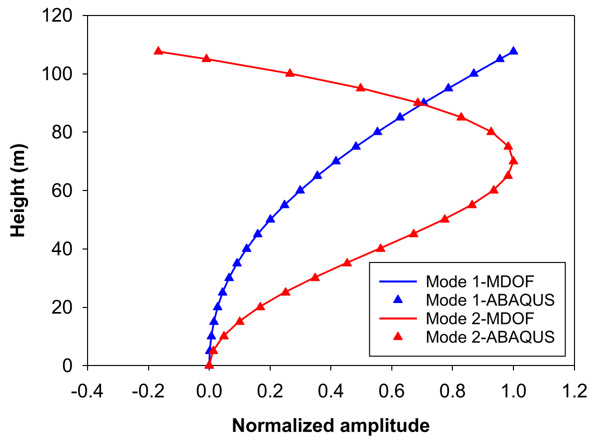

Fig. 2. Comparison of mode shapes of the tower between the MDOF and ABAQUS models.

2.2. SPAMD

2.2.1. System configuration and working mechanism

Fig. 4 shows the schematic of the SPAMD system, and it can be inferred that the SPAMD evolves from the self-powered active controller (SPAC) prototype (i.e., bottom right part of Fig. 4) that had been previously investigated in [35] and [36]. However, in contrast to the two-node device (i.e., SPAC) that responds to the relative motion between its two end nodes, the proposed SPAMD shown in Fig. 4 connects the SPAC to an auxiliary mass in the similar configuration of a classical active mass damper (AMD). As such, on the one hand, compared with a conventional AMD, the original actuator is replaced by the SPAC which allows for a potential self-powered feature without compromising the active control performance. On the other hand, the addition of mass transforms the original two-node device (i.e., SPAC) to a single-node device which significantly widens its application range (e.g., OWTs in the present study). It should be noted that the terms "single-node" and "double-nodes" reflect if the device shall require a single-end connection or both ends connected under normal operation.

In terms of SPAC, it comprises three major modules, namely, the EM transducer module, the H-bridge module, and the controller module. In brief, the EM transducer module oversees the conversion between electrical energy and structural kinetic energy. For a non-commutated direct-current EM transducer as adopted in the present study, we have

$$\begin{cases} V_{\mathrm{em}} = K_{\mathrm{em}}\dot{x}_{\mathrm{em}} \\ f_{\mathrm{ctrl}} = -K_{\mathrm{em}}i \end{cases} \tag{5}$$

where K_{em} is known as the motor constant being an inherent fixed-value parameter of the EM transducer once manufactured, $\dot{x}_{\mathrm{em}}$ is the relative velocity between the two nodes of the EM transducer (i.e., the relative velocity between the mass ($\dot{x}_a$) and the nacelle ($\dot{x}_{43}$, defined in Section 2.1) in the present study), i is the current flowing through the EM transducer, and V_{em} and f_{ctrl} are the counter-electromagnetic force (counter-*emf*) and the generated control force, respectively.

The H-bridge module is made up of four metal-oxide-semiconductor field-effect transistors (MOSFETs) and functions as the interface between the EM transducer module and the energy pool (i.e., the rechargeable battery in Fig. 4). The diagonal MOSFET sets are controlled by the same signal (i.e., either Sig 1 for M1 and M4, or Sig 2 for M2 and M3) and essentially function as fast-alternating switches. Thus, by assigning corresponding complementary pulse-width modulation (PWM) signals (i.e., when one sequence is high, the other sequence is correspondingly low) operating at hundreds or thousands of Hertz, there will be two connection modes (Mode ① and Mod ② in Fig. 4) showing up in an alternating manner. Therefore, under respective Mode ① and Mode ②, we have

$$V_{\mathrm{em}} - V_{\mathrm{batt}} - iR_{\mathrm{t}} - L_0\frac{di}{dt} = 0 \text{ when } 0 < t < t_1 \tag{6}$$

$$V_{\mathrm{em}} + V_{\mathrm{batt}} - iR_{\mathrm{t}} - L_0\frac{di}{dt} = 0 \text{ when } t_1 < t < T_{\mathrm{PVM}} \tag{7}$$

where V_{em} is the counter-*emf*, V_{batt} is the voltage of the rechargeable

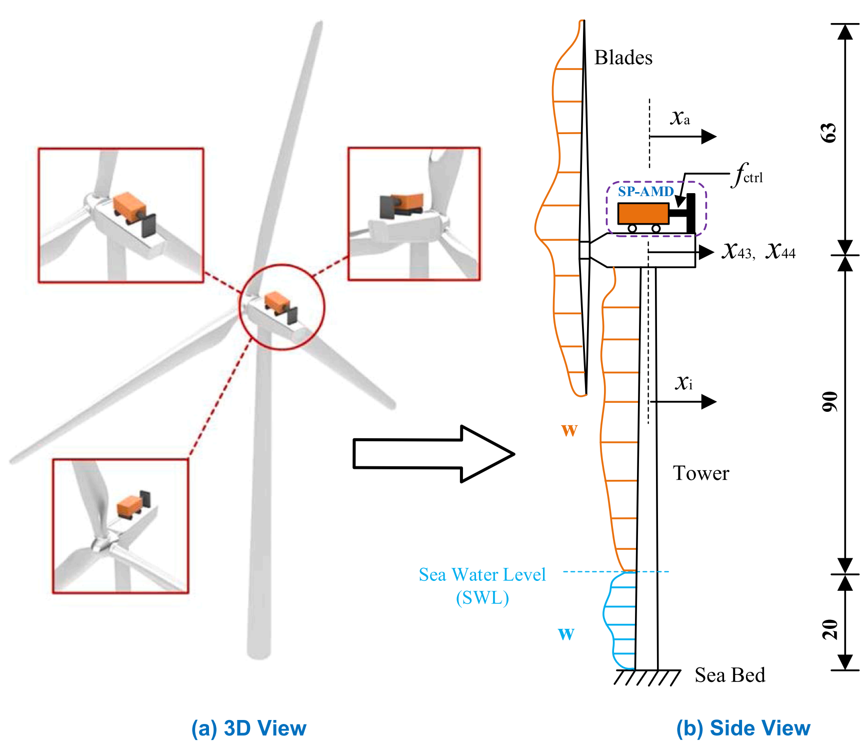

Fig. 3. Schematic of OWT with SPAMD (Unit in m).

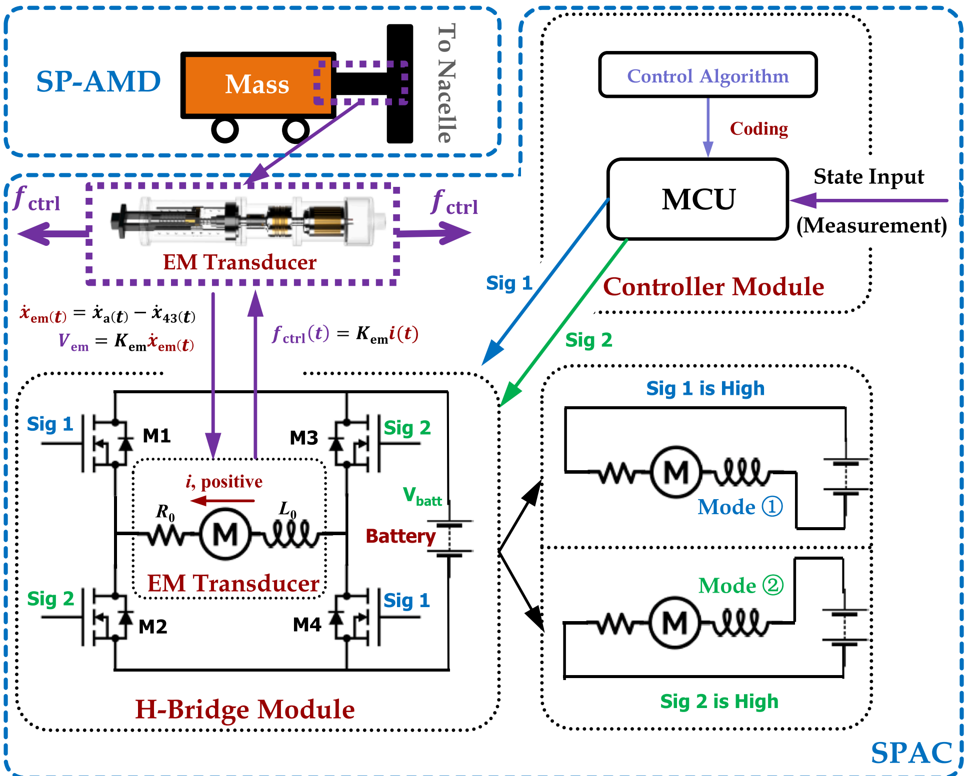

Fig. 4. Configuration of SPAMD.

battery, i is the current flowing through the EM transducer that is equal in magnitude to that through the battery, R_t is the total circuit resistance including motor inner resistance (i.e., R_0), connection wire resistance, battery inner resistance, etc., L_0 is the motor's inner inductance, t_1 corresponds to the duration when Sig 1 is high and Sig 2 is low within one PWM period (i.e., T_{PVM}).

In addition, given the current flowing through the motor inner inductance cannot experience abrupt change, and the absolute change amplitude within one PWM cycle (a complete set of Mode ① and Mode ②) shall equal to zero which will otherwise accumulate energy at the inductor position, we can derive

$$i = \frac{V_m + V_{batt}(1 - 2D_1)}{R_t} \tag{8}$$

from Eqs. (6) and (7), where V_m is the motor voltage induced by the relative motion between the active mass and the nacelle and D_1 is defined as the duty cycle of Sig 1 in the form of $D_1 = t_1/T_{PVM}$ (i.e., that of Sig 2 automatically turns out to be $D_2 = 1 - D_1$, since Sig 1 and Sig 2 are complementary PWM signals sequences to each other). By further substituting Eq. (8) into Eq. (5), we have

$$f_{ctrl} = -K_{em}\left[\frac{K_{em}\dot{x}_{em} + V_{batt}(1 - 2D_1)}{R_t}\right] \tag{9}$$

Eq. (9) essentially reveals that, since all parameters other than D_1 can be regarded as constants within one PWM cycle (i.e., extremely short duration), the control force is solely proportional to D_1. That is, by assigning the corresponding duty cycle following the control algorithm, we can enable the SPAMD system to generate the desired active control force linearly.

The remaining controller module is substantially made up of a micro-controller unit (MCU) with (1) computation and processing ability, (2) A/D conversion ability, and (3) signal input/output ability. It will intake the measurement, process the data based on the pre-coded control algorithm, and generate PWM signals to the H-bridge. Once the instant control force (f_{ctrl}) is determined from the control algorithm, the corresponding duty cycle of the PWM signals to be output by the MCU can be subsequently obtained based on Eq. (8) as

$$D_1 = \frac{1}{2} + \frac{V_m - f_{ctrl}R_t/K_{em}}{2V_{batt}} \tag{10}$$

2.2.2. Power analysis

Based on the above introduction, the proposed SPAMD can provide simultaneous energy harvesting and actuation abilities and thus makes the corresponding analysis of its energy issue an important task to realize self-powered active control. By recalling its working mode depicted in Fig. 4, and following the same sign definitions (i.e., current/voltage), we learned the circuit current flows into the battery in Mode ① (i.e., charging process, $0 - t_1$) and out of the battery under Mode ② (i.e., consuming process, $t_1 - T_{PWM}$). Consequently, the normalized instant power of the SPAMD can be derived as

$$P_E = V_{batt}i(2D_1 - 1) \tag{11}$$

By further substituting Eqs. (8) and (9) into the above equation, we can obtain

$$P_E = V_m i - i^2 R_t = -f_{ctrl}\dot{u} - i^2 R_t \tag{12}$$

which essentially confirms the satisfaction of the energy conservation requirement by stating that harvested energy shall equal the external energy input minus the energy portion dissipated into ambient heat. Thus, to ensure the successful realization of the expected long-term self-powered active control, we will simply make sure the harvested energy (E) is positive within an interested duration ($t_1, t_1 + \tau$). That is,

$$E = \int_{t_1}^{t_1+\tau} P_E \cdot dt = \int_{t_1}^{t_1+\tau} \left(V_m i - i^2 R_t\right) \cdot dt = \int_{t_1}^{t_1+\tau} \left(-f_{ctrl}\dot{u} - i^2 R_t\right) \cdot dt > 0 \tag{13}$$

From the energy perspective, the proposed device will allow for energy exchange/manipulation between the OWT (target structural kinetic energy) and the energy pool (i.e., electrical energy of the rechargeable battery set). Ideally, perfect vibration control indicates a total still of the structure without any external energy injection from the wind/wave disturbances. Thus, in theory, no external energy shall be required to achieve optimal control. Currently, the high-power consumption of the active controller owes to the energy required to be exerted back to the structure fulfilling the hysteresis loop requested by the control algorithm, and high energy-dissipation of the structural kinetic energy into ambient heat. Nevertheless, the proposed SPAMD can simultaneously function as a force-tracking actuator and energy harvester. Instead of transforming the structural kinetic energy into ambient heat, the SPAMD can temporarily store such energy that will be subsequently used to compensate for the actuation energy demand and consequently achieve an authentic self-powered active control of the OWT.

2.3. Energy-adaptive self-powered active control to OWT using SPAMD

A modified Linear Quadratic Gaussian (LQG) control with a variable gain matrix regulated by the energy index is adopted in the present study to realize adaptive optimal active control while maintaining the system self-powered.

Fig. 5 provides the block diagram of such a system from which three major modules can be subsequently identified and marked using dashed frames. From top to bottom, they are (1) the OWT plant module, (2) the SPAMD module, and (3) the estimator module, respectively. Notably, considering space constraints in OWTs, the maximum working displacement of the proposed SPAMD is designed as the diameter at the top of the tower (i.e., 3.87 m as shown in Table 1), and thus two corresponding blocks limiting excessive force and displacement are added in Fig. 5.

Specifically, the OWT plant module essentially denotes the wind turbine that has been depicted in the state-space form based on Eqs. (3) and (4) as

$$\begin{cases} \dot{z} = Az + B_c f_{\mathrm{ctrl}} + B_w w \\ y = H_1 z + v \end{cases} (\text{Continuous } form) \tag{14}$$

$$\begin{cases} z[n+1] = Az[n] + B_c f_{\mathrm{ctrl}}[n] + B_w w[n] \\ y[n] = H_1 z[n] + v[n] \end{cases} (\text{Discrete } form)$$

where $z = \begin{bmatrix} x & \dot{x} \end{bmatrix}^T$ is the state vector; v is the measurement noise, respectively; n is the time step; A, B_c, B_w, and H_1 are the system matrix, control force input matrix, wind force input matrix, and observer matrix, which are in the form of

$$A_{90\times 90} = \begin{bmatrix} 0_{45\times 45} & I_{45\times 45} \\ -M^{-1}K & -M^{-1}C \end{bmatrix}, B_c = \begin{bmatrix} 0 \\ M^{-1}\gamma \end{bmatrix}, B_w = \begin{bmatrix} 0 \\ M^{-1}I_{n\times n} \end{bmatrix}, H_1 = \begin{bmatrix} h_{1,1} & h_{1,2} & \cdots & h_{1,90} \\ h_{2,1} & h_{2,2} & \cdots & h_{2,90} \\ \vdots & \vdots & \ddots & \vdots \\ h_{10,1} & h_{10,2} & \cdots & h_{10,90} \end{bmatrix} \tag{15}$$

It needs to clarify that, for a non-fully observable system (i.e., the OWT consisting of 44 DOFs in the present study), the observer matrix H_1 is adopted to obtain the best-guessed full-state vector, and thus a full-state Linear Quadratic Regulator (LQR) control can be implemented. Herein, if the sensors are designated to be deployed at the 0.25H, 0.5H, 0.75H, and H locations (H is the tower height) as requested by the designed LQG control algorithm, then the H_1matrix has $h_{1,10} = h_{2,21} = h_{3,32} = h_{4,43} = h_{5,45} = h_{6,55} = h_{7,66} = h_{8,77} = h_{9,88} = h_{10,90} = 1$, whereas all the other elements shall equal zero.

Similarly, the state-space representation of the estimator can be written as

$$\dot{\hat{z}} = A\hat{z} + B_c f_{\mathrm{ctrl}} + L(y - \hat{y}) \ (\text{Continuous } form) \tag{16}$$

$$\hat{z}[n+1|n] = A\hat{z}[n|n-1] + B_c f_{\mathrm{ctrl}}[n] + L(y[n] - H\hat{z}[n|n-1]) \ (\text{Distrete } form)$$

where $\hat{z}$ is the estimated full-state vector, $\hat{y} = H_1\hat{z}$ is the estimated output vector, and L is the observer gain that equals to

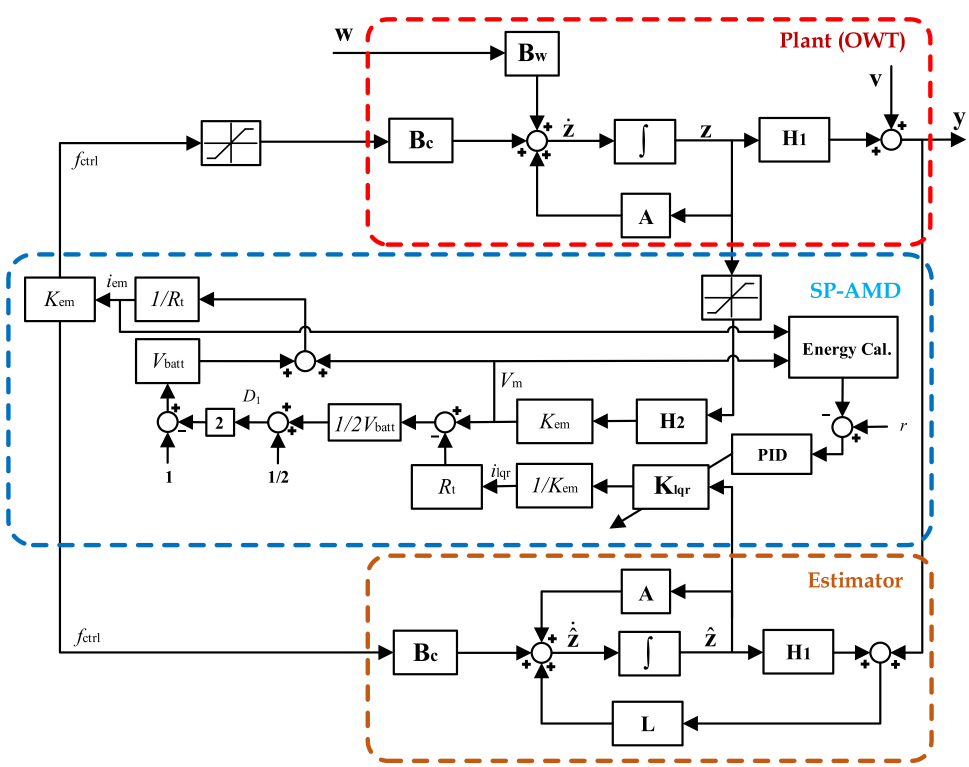

Fig. 5. Block diagram of OWT with SPAMD system.

$$L = (PH_1^T + B_w N)V^{-1} \quad (17)$$

where $N = E(wv^T)$ is the covariance of w and v, $V = E(vv^T)$ is the covariance of the measurement noise, P is the error covariance that can be computed by solving the Algebraic Riccati Equation (ARE)

$$AP + PA^T + B_w W B_w^T - PH_1^T V^{-1} H_1 P = 0 \quad (18)$$

where $W = E(ww^T)$. Consequently, $\hat{z}$ can be obtained by minimizing the following cost function:

$$J_1 = \lim_{t\to\infty} E[(z-\hat{z})(z-\hat{z})^T] \quad (19)$$

and the desired control force subsequently becomes

$$f_{ctrl} = K_{lqr}\hat{z} \quad (20)$$

where K_{lqr} is the LQR gain that minimizes another quadratic performance index J_2 in the form of

$$J_2 = \int_0^{\infty} (z^T Q z + f_{ctrl}^T R f_{ctrl}) dt \quad (21)$$

Similar to the calculation of estimator gain L, the K_{lqr} is calculated as

$$K_{lqr} = RB_c^T P_{lqr} \quad (22)$$

where P_{lqr} can be computed by solving the ARE of

$$A^T P_{lqr} + P_{lqr} A - P_{lqr} B_c R^{-1} B_c^T P_{lqr} + Q = 0 \quad (23)$$

In the present study, the K_{lqr} and L matrices are obtained using MATLAB *lqr* and *lqe* functions respectively. Nevertheless, referring to the calculation procedures above, these two matrices can be obtained by any computational module (e.g., a microcontroller unit) via the embedded ARE solver.

By further defining the error vector as $e = z - \hat{z}$ and substituting Eqs. (16), (20) into Eq. (14), the state-space representation of the overall system can be obtained as

$$\begin{cases} \begin{bmatrix} \dot{z} \\ \dot{e} \end{bmatrix} = \begin{bmatrix} A - B_c K_{lqr} & B_c K_{lqr} \\ 0 & A - LH_1 \end{bmatrix} \begin{bmatrix} z \\ e \end{bmatrix} + \begin{bmatrix} B_w & 0 \\ B_w & -L \end{bmatrix} \begin{bmatrix} w \\ v \end{bmatrix} \\ y = [H_1 \quad 0] \begin{bmatrix} z \\ e \end{bmatrix} \end{cases} \quad (24)$$

Thus far, the wind turbine system under the conventional LQG control using the proposed SPAMD has been well established, only that the self-powered feature of SPAMD cannot be always guaranteed in the long run within the current framework. Consequently, we further introduce a second-tier feedback loop that brings the energy index into consideration. It will periodically adjust the K_{lqr} value in the long run that balances the energy harvesting and optimal control performances. In specific, the Energy Cal. Block in the SPAMD module refers to Eq. (13) to calculate harvested/consumed energy of one period, and this value will subsequently adjust the R matrix seen in Eq. (21) of the next step as

$$R_{n+1} = R_n e^{-(K_p\delta + K_i \int_{t_1}^{t_1+\tau} \delta dt)} \quad (25)$$

where K_p and K_i are the proportional and integral coefficients of the PI controller in the exponential term, respectively. $\delta = E - r$ is the difference between the calculated energy and the reference value. Herein, the r value can be selected as either zero or an appropriate positive number to ensure an overall energy-neutral/harvesting effect via the proposed SPAMD system. Note if a net positive power (i.e., harvested power) is chosen, it can potentially supply the sensors in the ambient environment that further facilitate the structural health monitoring function. The H2 block in Fig. 5 extracts the relative velocity between the two nodes of the EM transducer (i.e., the relative velocity between active mass and the nacelle), and the rest of the blocks in the SPAMD module reflects the relations introduced in Eq. (10).

3. Wind and sea wave loads

Wind loads acting on the rotating blades and tower are simulated in FAST. The simulation procedures are briefly summarized as follows, and interested readers can refer to Ref. [40] for more detailed information. First, a stochastic, full-field, and turbulent wind is generated in TurbSim, which is the pre-processing module in FAST. The Kaimal spectrum [41] is used to describe the power spectral density (PSD) function of the fluctuating wind speed, and certain similarities of the wind speed along the height direction are considered by the spatial coherency loss function [41]. Then, the NREL 5 MW OWT is built in FAST, and wind loads on the tower and rotating blades can be calculated via the internal subroutine AeroDyn using the blade element momentum method [42] according to the three-dimensional wind profile generated by the TurbSim simulator. Subsequently, wind load time histories along the tower and blades are extracted and applied to corresponding locations in the developed model. Notably, because the blades are not explicitly modeled in the present study, resultant forces and moments at the root of the blades are applied at the top of the tower.

The control effectiveness of the proposed energy-adaptive SPAMD is investigated with four mean wind speeds, namely 8 m/s, 11.4 m/s, 16 m/s, and 25 m/s, which are within the cut-in and cut-out wind speeds of the NREL 5 MW OWT as shown in Table 1, and the turbulence intensity is 12%. As mentioned above, the pitch control is activated to change the pitch angle when the wind speed is above the rated wind speed, and the variation of pitch angle is considered in the wind speed and wind load simulations in the present study. In addition, the wind speeds and loads are simulated with a time duration of 500 s and a fixed time interval of 0.05 s Fig. 6 shows the wind speed and wind load (which come from the rotor) in the fore-aft direction at the tower top under the rated wind speed of 11.4 m/s, and the wind speeds and wind loads under the other three mean wind speeds are not presented for conciseness.

The JONSWAP spectrum in conjunction with the inverse fast Fourier transform is used to determine the sea surface elevation, and the sea wave loads acting on the monopile foundation are calculated by the Morison equation [40]. The significant wave height and peak wave period of 6 m and 10 s are used in the present study. Fig. 7(a) compares the simulated PSD of the sea surface elevation with the given model (i.e., the JONSWAP spectrum), and the sea wave load per unit length at the mean seawater level is shown in Fig. 7(b).

Considering OWTs located in ocean areas, the combined wind and sea wave loads are applied to different locations along the height of OWTs. In the present study, the wind loads are applied to the tower (from 20 m to 107.6 m as shown in Figs. 1 and 3), and the sea wave loads are applied to the monopile foundation (from 0 to 20 m).

4. Results and discussion

4.1. Numerical simulation results

This section provides simulation results that highlight the merits of the proposed SPAMD in comparison to a typical optimal TMD and the uncontrolled scenarios. Meanwhile, the self-powered feature is specifically emphasized.

The mass ratios (μ) of both the SPAMD and the TMD are set as 3% of the first modal mass of the OWT (1.2718×10^4 kg). Referring to the optimal design of TMD [43], the optimal frequency ratio (γ_{TMD}) and damping ratio (ζ_{TMD}) can be computed as 0.9781 and 0.0856, respectively, based on the equations below:

$$\gamma_{TMD} = \frac{\sqrt{1+\mu/2}}{1+\mu} \quad (26)$$

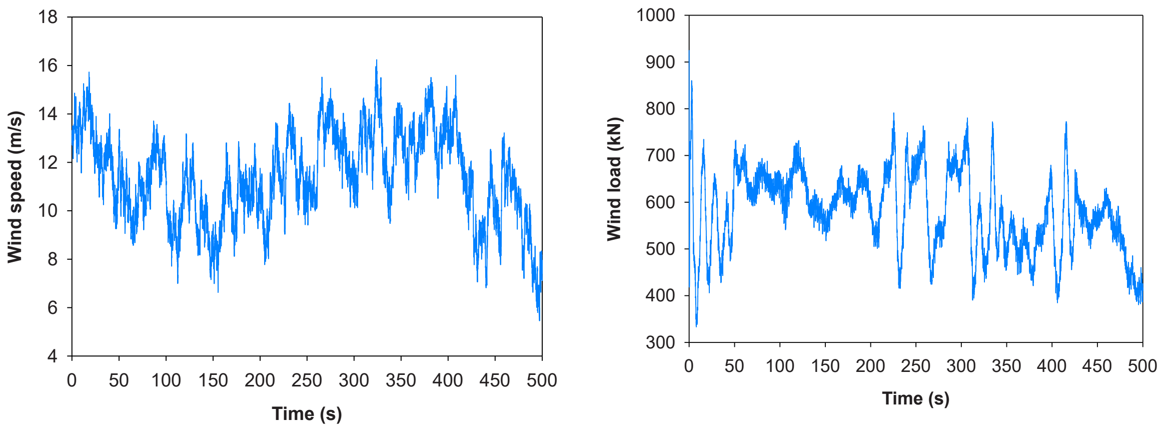

(a) Wind speed

(b) Wind load

Fig. 6. Wind information at the tower top under the rated wind speed of 11.4 m/s.

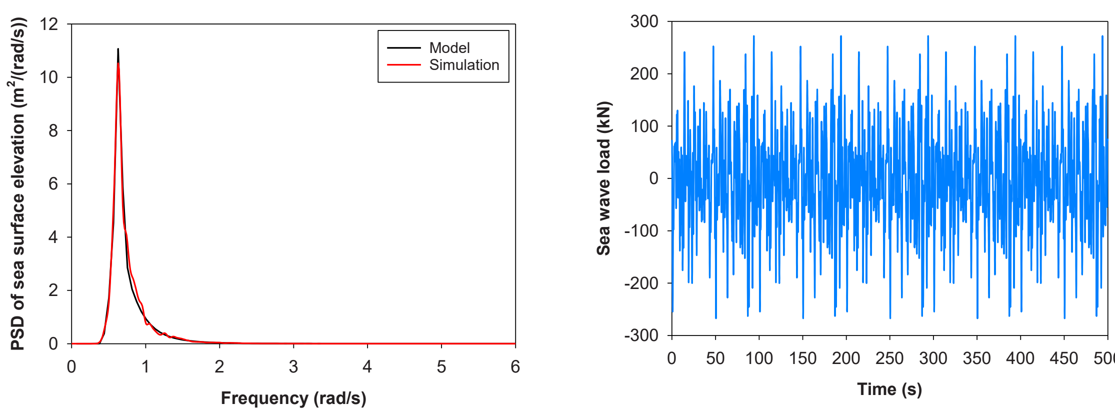

(a) PSD of sea surface elevation

(b) Sea wave load at the mean seawater level

Fig. 7. Sea wave information.

$$\zeta_{\mathrm{TMD}} = \sqrt{\frac{\mu(1+3\mu/4)}{4(1+\mu)(1+\mu/2)}} \tag{27}$$

Consequently, the spring stiffness (k_{TMD}) and damping coefficient (c_{TMD}) can be determined as $3.7929\times10^{4}\mathrm{N/m}$ and $3.7621\times10^{3}\mathrm{N/(m/s)}$, respectively, via the equations below:

$$k_{\mathrm{TMD}} = m_{\mathrm{TMD}}(\gamma_{\mathrm{TMD}}\omega_s)^2 \tag{28}$$

$$c_{\mathrm{TMD}} = 2m_{\mathrm{TMD}}\zeta_{\mathrm{TMD}}\gamma_{\mathrm{TMD}}\omega_s \tag{29}$$

where m_{TMD} is the TMD mass, and ω_s is the first modal frequency of the OWT (i.e., 1.7658 rad/s as given in Table 2).

Figs. 8 and 9 provide the time histories of acceleration and displacement of the tower top under various control scenarios (i.e., uncontrolled, with TMD, with SPAMD) and serving conditions (i.e., different wind speeds) whose details can be found in the corresponding captions. Compared with the uncontrolled case, both TMD and SPAMD bring substantial vibration suppression effects to the tower; and between these two, SPAMD achieves comparably better control performance than TMD by imposing active control. Notably, neither of these two approaches requires external energy input. Quantitative results (i.e., steady state root-mean-square (RMS) acceleration and displacement responses of the tower top in a period of 100–500 s, and the first 100 s are not considered to eliminate the transient responses) are subsequently shown in Figs. 10 and 11. It needs to justify that overturning is a critical issue in the foundation design and analysis of OWTs, and a maximum tilt angle of 0.5° was reported in [44], which can be converted to a displacement of 0.94 m at the tower top. As shown in Fig. 9, the maximum displacement at the tower top is approximately 0.476 m in 100–500 s, which is smaller than the allowable displacement/tilt angle. Moreover, when TMD and SPAMD are installed, the displacements of the tower are further reduced. Therefore, the overturning effect is not addressed herein.

As shown in Figs. 10 and 11, in terms of RMS accelerations and displacements, both TMD and SPAMD achieve the maximum reduction ratios under the wind speed of 25 m/s, which is taken as an example for detailed analyses. The calculated RMS accelerations of the uncontrolled, with TMD, and with SPAMD conditions are 0.473 $\mathrm{m/s^2}$, 0.252 $\mathrm{m/s^2}$, and 0.160 $\mathrm{m/s^2}$, respectively, and the RMS displacements are 0.154 m, 0.086 m, and 0.052 m, respectively. These results indicate a net 46.7% reduction in the RMS acceleration and 44.0% reduction in the RMS displacement by using TMD compared with the uncontrolled scenario, and an extra 19.4% for acceleration and 22.5% for displacement are

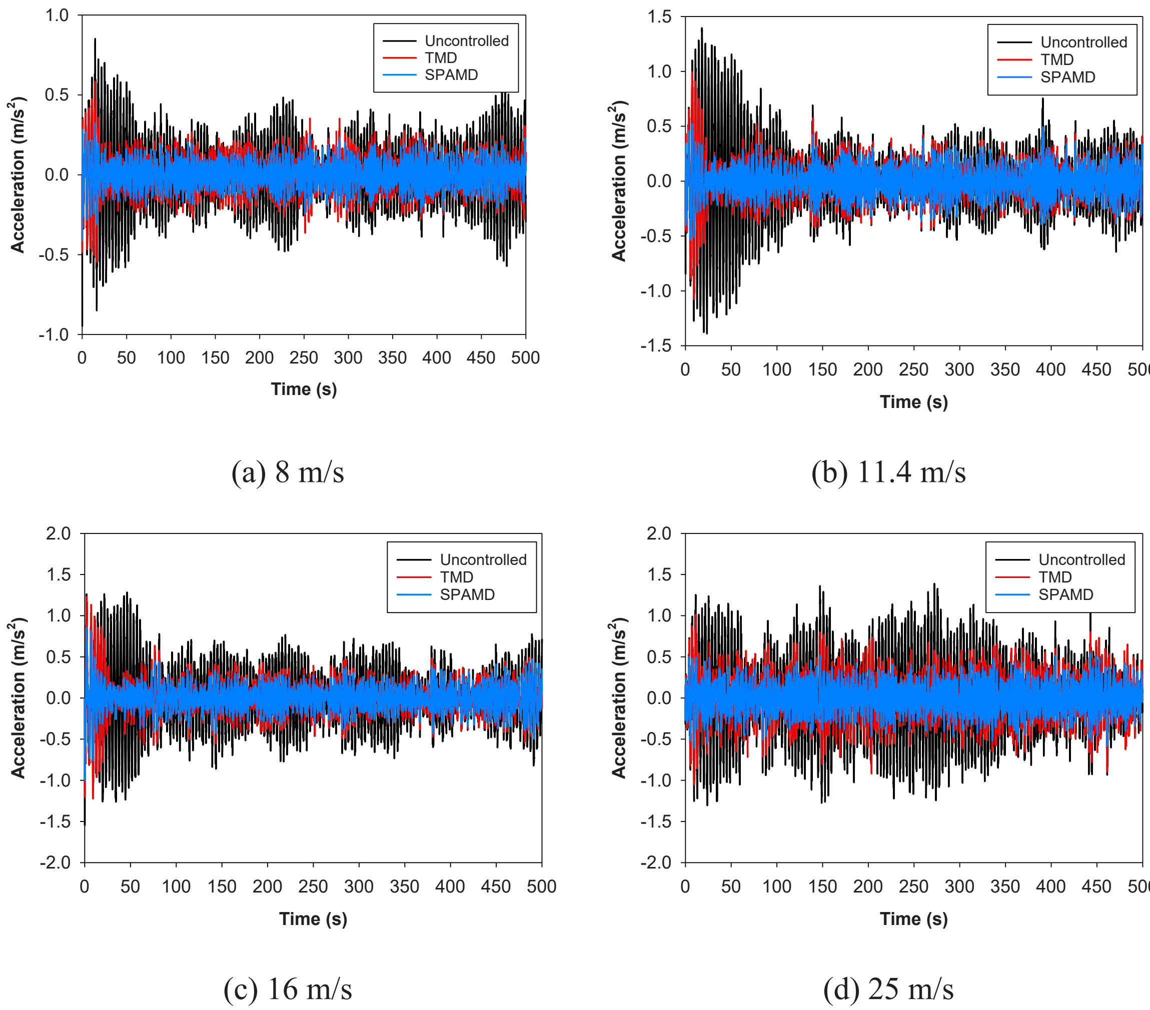

Fig. 8. Time histories of acceleration at the tower top.

granted by the proposed SPAMD over TMD. That is, a total of 66.1% vibration reduction for acceleration and 66.5% reduction for displacement are successfully achieved by SPAMD which features its superior control performance while requiring no external energy input as a pseudo-passive device. The parallel comparison among responses under different wind speeds also suggests that SPAMD enhances its performance as wind speed increases, which also matches the desired control philosophy – best control is expected under worst serving conditions. This "adaptive" feature also makes SPAMD a promising control device for OWTs.

In terms of the evaluation of system energy to highlight the self-powered feature, Fig. 12 provides the time-domain diagram containing both the instant mean power (i.e., every 5 s corresponding to one iteration in the present study) in the blue rectangular dot line and the **R**-value in the LQG control in red round dot line. Notably, only the instant mean power and **R**-value under the rated wind speed of 11.4 m/s are presented in Fig. 12 for discussions and the results of the other mean wind speeds are not shown for conciseness. The blue dots (i.e., instant power) fluctuate around the zero line, which reflects the adaptive feature of the proposed system that can ensure a long-term self-powered control requirement as featured in Eq. (25).

In particular, the energy-adaptive self-powered active control requires real-time adjustment on the **R**-value based on the energy term following the PID control algorithm. That is, positive accumulated average energy from the previous iterations will result in a more "aggressive" control effort and thus reduce the chance of harvesting energy from the host structure. Therefore, in the next step, the system will likely experience a net energy consumption (or lower harvested energy), which will then increase the **R**-value and reduce the control effort in the next round. As such, the system will remain at an average zero value while outputting continuous energy- adaptive optimal control performance.

4.2. Potential challenges

The proposed SPAMD builds upon prior work by the research group [35,36]. However, it is worth noting that the existing prototype referenced in [35,36] is of a small-scale nature, primarily designed for experimental validation to demonstrate its initial feasibility. Scaling up this device for large-scale applications, such as deploying it to OWTs in the present study, presents several potential challenges:

(1) High Operation Voltage and Current: Large-scale deployment is expected to demand higher operation voltage and current. To address this, there may be a need to upgrade compatible electrical components. For instance, insulated-gate bipolar transistors could be considered replacements for MOSFETs to manage potential high-voltage spikes. Additionally, exploring the use of durable rechargeable batteries or specially designed capacitors could be necessary to meet the continuous demand for substantial energy exchange.
(2) Electromagnetic Transducer Modification: The electromagnetic transducer used in this paper is a two-dimensional direct-current non-commutated motor. For high-power applications, it may be

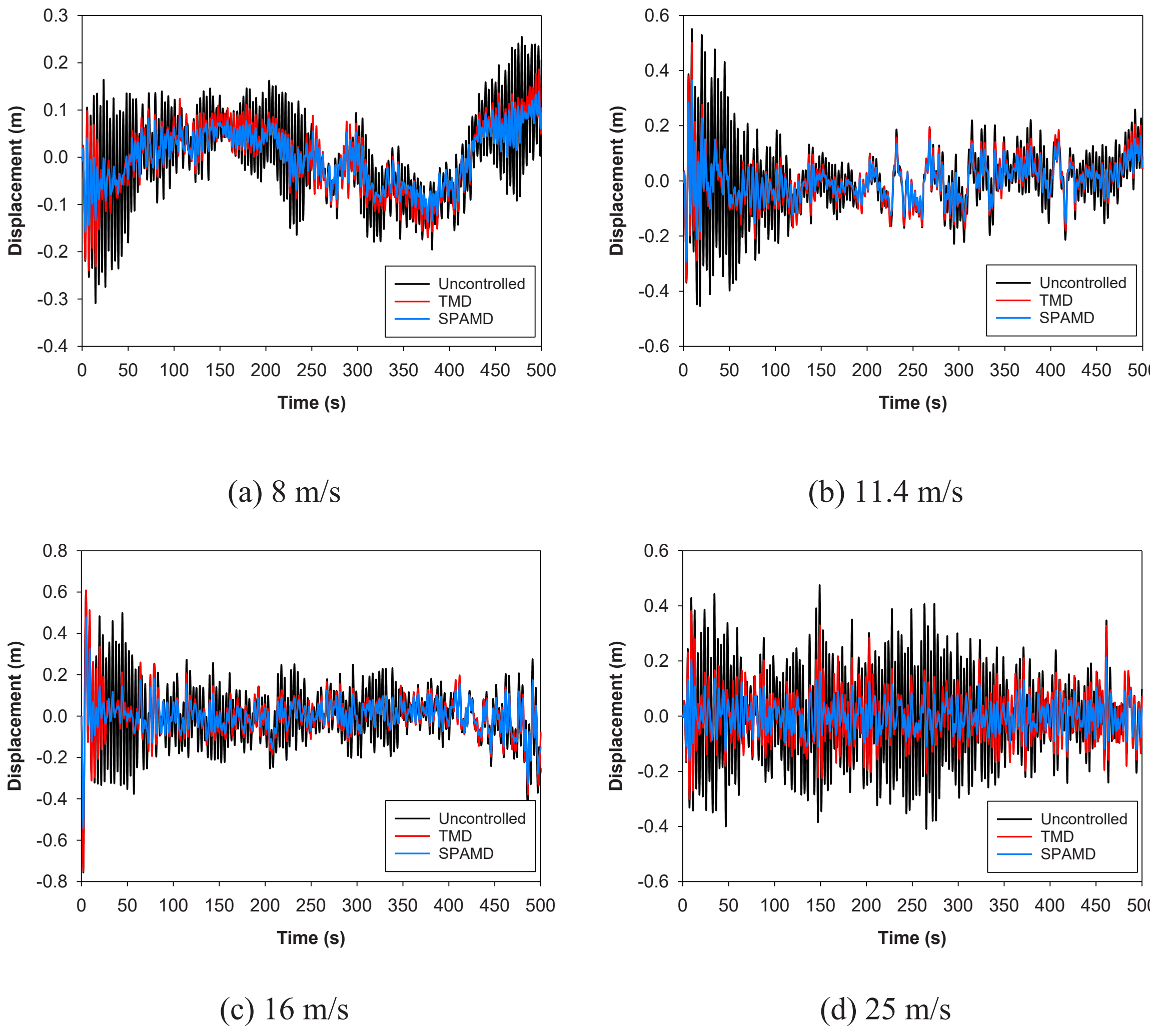

Fig. 9. Time histories of displacement at the tower top.

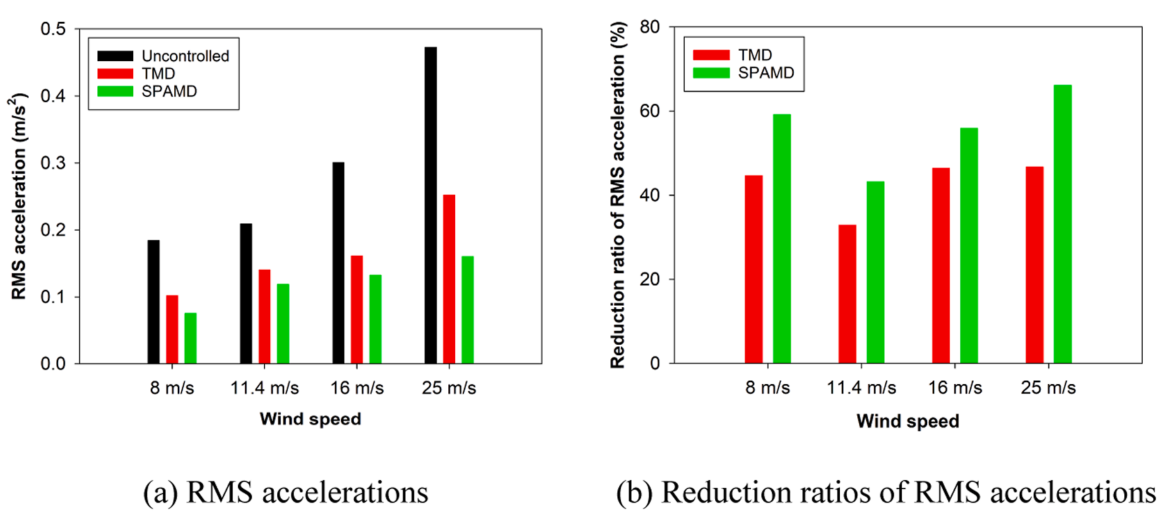

Fig. 10. RMS accelerations and corresponding reduction ratios.

more practical to consider replacing it with a three-phase electromagnetic transducer. However, such a modification would entail changes to both the H-ridge circuit topology and the corresponding control algorithm, necessitating further in-depth consideration. These challenges should be addressed when transitioning from small-scale prototypes to large-scale real-world applications.

(3) Economic Consideration: Compared with existing mature passive control techniques, the research and development cost (e.g., developing new control algorithms, circuit topologies, and

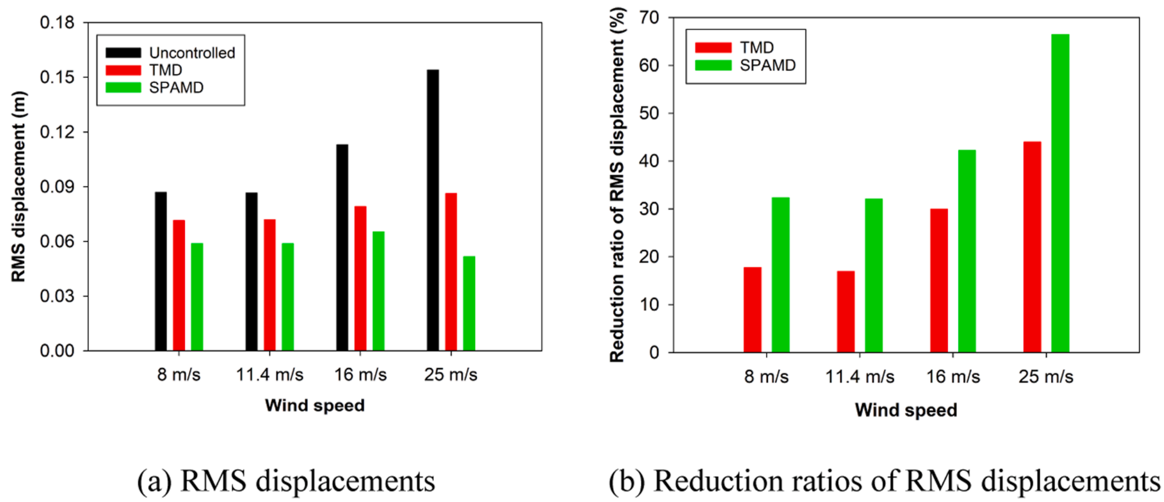

Fig. 11. RMS displacements and corresponding reduction ratios.

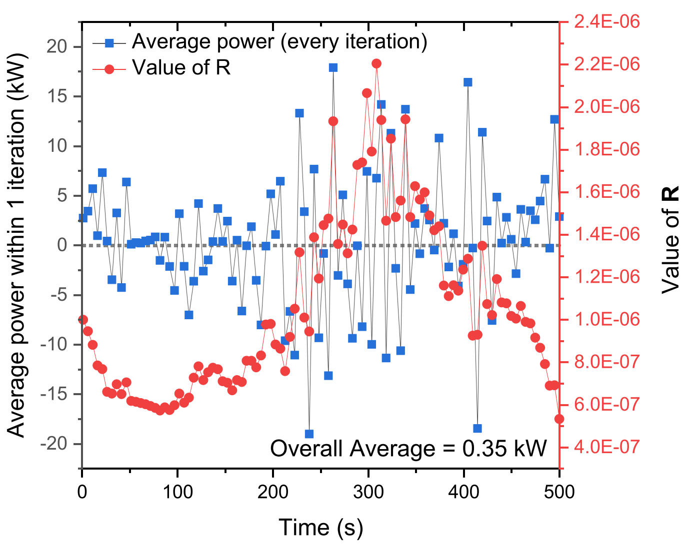

Fig. 12. Instant mean power (one iteration, 5 s in the present study) and value of **R** (of LQG) in the time domain.

system integration strategies), manufacturing and production costs, installation and maintenance costs should all be well considered and counted in the long-term return on investment calculation, to justify its feasibility to be practically deployed. Besides, regulatory and incentive considerations (e.g., renewable energy credits) could also positively affect the economic feasibility of SPAMD, yet negative regulatory hurdles or compliance costs can increase the economic challenges.

5. Conclusions

This paper proposes a novel energy-adaptive SPAMD system and subsequently discusses its feasibility of controlling a full-scale benchmark OWT for the first time. Although it may still take some extra time before its final applications to full-scale structures for potential economical and industrialization optimizations, the highlighted advantages of the proposed SPAMD in comparison to existing control technologies to OWTs are:

(1) It can perform adaptive full-loop active control (i.e., providing multi-mode control) to OWTs. This can be especially meaningful given the current trend of deploying OWT to further offshore regions where the service conditions may be harsh (e.g., typhoon, tsunami) and have more chances of experiencing higher modes vibration (2nd, 3rd, etc.).
(2) The simulation results suggest that SPAMD achieves better control performance under larger wind speed conditions. The reduction ratios of RMS accelerations and displacements are within the ranges of 43%–66% and 32%–66%, respectively, by using SPAMD in the investigated wind speeds. Moreover, SPAMD outperforms an optimally designed TMD and additional improvement is achieved depending on the wind speeds and responses.
(3) SPAMD remains self-powered at all times which eases the two major concerns regarding active control, namely, the high energy consumption and the potential instability.
(4) The proposed SPAMD is universally flexible, and can readily adapt other control algorithms (e.g., skyhook, sliding-mode control, etc.) or be applied to other structures (e.g., buildings and bridges subject to wind and earthquake loads, etc.) whenever found appropriate. Its intrinsic computation power enables it with the potential to further incorporate structure health monitoring functions without requiring additional power or sensors.

Given the increasing emphasis on green energy and sustainable society that accelerates the implementation of wind turbines, the proposed SPAMD is considered a promising candidate for the next-generation wind turbine control device, however, performing experimental tests of wind turbines with SPAMD to confirm its control effectiveness is worthwhile and will be investigated in future studies.

CRediT authorship contribution statement

LI Jin-Yang: Writing – review & editing, Writing – original draft, Validation, Software, Project administration, Methodology, Investigation, Funding acquisition, Formal analysis, Conceptualization. **ZHU Songye:** Writing – review & editing, Supervision, Project administration, Funding acquisition, Conceptualization. **Zhang Jian:** Software, Investigation, Formal analysis. **MA Ruisheng:** Investigation, Formal analysis. **Haoran Zuo:** Writing – review & editing, Writing – original draft, Validation, Project administration, Methodology, Investigation, Funding acquisition, Formal analysis, Conceptualization.

Declaration of Competing Interest

The authors declare that they have no known competing financial interests or personal relationships that could have appeared to influence the work reported in this paper.

Data availability

Data will be made available on request.

Acknowledgments

The authors would like to acknowledge the financial support from the Dalian University of Technology (DUT23RC(3)032), the State Key Laboratory of Coastal and Offshore Engineering (LY2302), the NSFC/RGC Collaborative Research Scheme (No. CRS_PolyU503/23, 52321165649), the National Natural Science Foundation of China (No. 52108479), and the Hong Kong Polytechnic University (1-YXB9).

References

[1] GWEC. Global wind report 2023. 2023.
[2] Zuo H, Bi K, Hao H. A state-of-the-art review on the vibration mitigation of wind turbines. Renew Sust Energ Rev 2020;121:109710.
[3] Lackner MA, Rotea MA. Passive structural control of offshore wind turbines. Wind Energy 2011;14:373–88.
[4] Zhang Z, Staino A, Basu B, Nielsen SR. Performance evaluation of full-scale tuned liquid dampers (TLDs) for vibration control of large wind turbines using real-time hybrid testing. Eng Struct 2016;126:417–31.
[5] Colwell S, Basu B. Tuned liquid column dampers in offshore wind turbines for structural control. Eng Struct 2009;31:358–68.
[6] Hemmati A, Oterkus E, Khorasanchi M. Vibration suppression of offshore wind turbine foundations using tuned liquid column dampers and tuned mass dampers. Ocean Eng 2019;172:286–95.
[7] Sun C, Jahangiri V. Bi-directional vibration control of offshore wind turbines using a 3D pendulum tuned mass damper. Mech Syst Signal Proc 2018;105:338–60.
[8] Sun C, Jahangiri V. Fatigue damage mitigation of offshore wind turbines under real wind and wave conditions. Eng Struct 2019;178:472–83.
[9] Jahangiri V, Sun C. Integrated bi-directional vibration control and energy harvesting of monopile offshore wind turbines. Ocean Eng 2019;178:260–9.
[10] Jahangiri V, Sun C, Kong F. Study on a 3D pounding pendulum TMD for mitigating bi-directional vibration of offshore wind turbines. Eng Struct 2021;241:112383.
[11] Liu X, Xu J, He G, Chen C. Lateral vibration mitigation of monopile offshore wind turbines with a spring pendulum pounding tuned mass damper. Ocean Eng 2022;266:112954.
[12] Liu G, Lei Z, Wang H. Investigation and optimization of a pre-stressed tuned mass damper for wind turbine tower. Struct Control Health Monit 2021:e2894.
[13] Lei Z, Liu G, Wen M. Vibration attenuation for offshore wind turbine by a 3D prestressed tuned mass damper considering the variable pitch and yaw behaviors. Ocean Eng 2023;281:114741.
[14] Ding H, Chen Y-N, Wang J-T, Altay O. Numerical analysis of passive toroidal tuned liquid column dampers for the vibration control of monopile wind turbines using FVM and FEM. Ocean Eng 2022;247:110637.
[15] Zhang R, Zhao Z, Dai K. Seismic response mitigation of a wind turbine tower using a tuned parallel inerter mass system. Eng Struct 2019;180:29–39.
[16] Chen MZ, Li Z, Wang H, Hu Y. Seismic response mitigation of a wind turbine via inerter-based structural control. Bull Earthq Eng 2023;21:1361–88.
[17] Kampitsis A, Kapasakalis K, Via-Estrem L. An integrated FEA-CFD simulation of offshore wind turbines with vibration control systems. Eng Struct 2022;254:113859.
[18] Ghassempour M, Failla G, Arena F. Vibration mitigation in offshore wind turbines via tuned mass damper. Eng Struct 2019;183:610–36.
[19] Dai K, Huang H, Lu Y, Meng J, Mao Z, Camara A. Effects of soil-structure interaction on the design of tuned mass damper to control the seismic response of wind turbine towers with gravity base. Wind Energy 2020;24:323–44.
[20] Lin G-L, Lu L-Y, Lei K-T, Liu K-Y, Ko Y-Y, Ju S-H. Experimental study on seismic vibration control of an offshore wind turbine with TMD considering soil liquefaction effect. Mar Struct 2021;77:102961.
[21] Arrigan J, Huang C, Staino A, Basu B, Nagarajaiah S. A frequency tracking semi-active algorithm for control of edgewise vibrations in wind turbine blades. Smart Struct Syst 2014;13:177–201.
[22] Arrigan J, Pakrashi V, Basu B, Nagarajaiah S. Control of flapwise vibrations in wind turbine blades using semi-active tuned mass dampers. Struct Control Health Monit 2011;18:840–51.
[23] Fitzgerald B, Basu B. Cable connected active tuned mass dampers for control of in-plane vibrations of wind turbine blades. J Sound Vib 2014;333:5980–6004.
[24] Fitzgerald B, Basu B, Nielsen SRK. Active tuned mass dampers for control of in-plane vibrations of wind turbine blades. Struct Control Health Monit 2013;20:1377–96.
[25] Staino A, Basu B, Nielsen SRK. Actuator control of edgewise vibrations in wind turbine blades. J Sound Vib 2012;331:1233–56.
[26] Staino A, Basu B. Dynamics and control of vibrations in wind turbines with variable rotor speed. Eng Struct 2013;56:58–67.
[27] Sun C. Mitigation of offshore wind turbine responses under wind and wave loading: considering soil effects and damage. Struct Control Health Monit 2017:e2117.
[28] Sun C. Semi-active control of monopile offshore wind turbines under multi-hazards. Mech Syst Signal Proc 2018;99:285–305.
[29] Hemmati A, Oterkus E. Semi-active structural control of offshore wind turbines considering damage development. J Mar Sci Eng 2018;6:102.
[30] Sarkar S, Chakraborty A. Optimal design of semiactive MR-TLCD for along-wind vibration control of horizontal axis wind turbine tower. Struct Control Health Monit 2018;25:e2083.
[31] Saptarshi Sarkar A. Development of semi-active vibration control strategy for horizontal axis wind turbine tower using multiple magneto-rheological tuned liquid column dampers. J Sound Vib 2019;457:15–36.
[32] Fitzgerald B, Sarkar S, Staino A. Improved reliability of wind turbine towers with active tuned mass dampers (ATMDs). J Sound Vib 2018;419:103–22.
[33] Hu Y, Chen MZ, Li C. Active structural control for load mitigation of wind turbines via adaptive sliding-mode approach. J Frank Inst 2017;354:4311–30.
[34] Brodersen ML, Bjørke AS, Høgsberg J. Active tuned mass damper for damping of offshore wind turbine vibrations. Wind Energy 2017;20:783–96.
[35] Li J-Y, Zhu S. Self-powered active vibration control: concept, modeling, and testing. Eng 2022;11:126–37.
[36] Li J-Y, Zhu S. Tunable electromagnetic damper with synthetic impedance and self-powered functions. Mech Syst Signal Proc 2021;159:107822.
[37] Li J-Y, Shen J, Zhu S. Adaptive self-powered active vibration control to cable structures. Mech Syst Signal Proc 2023;188:110050.
[38] Jonkman J, Butterfield S, Musial W, Scott G. Definition of a 5-MW Reference Wind Turbine for Offshore System Development. Golden, Colorado: National Renewable Energy Laboratory; 2009.
[39] Chopra AK. Dynamics of Structures. fourth ed.,. New Jersey: Prentice Hall; 2012.
[40] Zuo H, Zhang J, Yuan GK, Zhu S. Wind-and sea wave-induced response mitigations of offshore wind turbines using track nonlinear energy sinks. Struct Control Health Monit 2022:e2990.
[41] IEC 61400-1. Wind Turbines-Part 1: Design requirements. third ed.,. Geneva, Switzerland: International Electrotechnical Commission; 2005.
[42] Moriarty PJ, Craig HA. AeroDyn Theory Manual No. NREL/EL-500-36881. Golden, Colorado: National Renewable Energy Laboratory; 2005.
[43] Warburton G. Optimum absorber parameters for various combinations of response and excitation parameters. Earthq Eng Struct Dyn 1982;10:381–401.
[44] DNV DNV-OS-J101: Design of offshore wind turbine structures. Denmark: Copenhagen, 2014.